Processing of Ultrafine/nano-grained microstructures through additive manufacturing techniques: a critical review

M.J. Gholamzadeh-Sarmi[1], S.M. Fatemi*[1,2], N. Mollaei[3], A. Abedi[1]

[1]Department of Metallurgy and Materials Engineering, Shahid Rajaee Teacher Training University, Tehran, Iran;

[2]Department of Materials Science and Engineering EEBE, Universidad Politécnica de Catalunya, c/Eduard Maristany 10-14, Barcelona 08019, Spain;

[3]School of Metallurgy and Materials Science, Iran University of Science and Technology, Tehran, Iran.

*Corresponding author email: seyed.mahmood.fatemi@upc.edu

ABSTRACT

Additive manufacturing (AM) has emerged as a transformative technology that produces complex, high-performance components, enabling unprecedented design flexibility and material efficiency. This paper explores the potential of additive manufacturing processes to produce ultrafine/nano-grained microstructures, which are characterized by superior mechanical properties, enhanced corrosion resistance, and improved thermal stability. The study delves into various AM techniques based on the physical phenomenon incorporated to additively bond the material portions. Accordingly, the reported results in the literature were reviewed by categorizing the methods into melting-based and deformation-based approaches and examining the conditions and parameters critical to achieving ultrafine/nano-grained microstructures. Key factors, including the optimization of process parameters as well as the specification of initial feedstock material, are discussed. This comprehensive review shows that in melting-based methods, lower power and higher scan speed result in reduced heat input, leading to smaller melt pools and faster solidification rates, which in turn produce finer grains. On the other hand, in deformation-based methods, smaller initial particle sizes and higher particle velocities generate greater impact energy, which can lead to grain size reduction. This review article also highlights the current potential and achievements in the field of additive manufacturing for producing ultrafine/nano-grained materials, which may contribute to the development of high-performance materials and components for the next generation.

Keywords: Additive manufacturing; Ultrafine/nano-grained; Grain refinement; Melting-based method; Deformation-based method.

1. Introduction

Additive manufacturing (AM) can be described as a technique of bonding materials through fusion, sintering, binding, or solidifying material feedstocks such as wires, powders, and liquid resin. AM processes invoke the modeling of components using 3D computer data or standard tessellation language (STL) files, which simulate the addition of material to the base in a layer-by-layer fashion.

The advantages of AM over conventional methods have made it popular in many industries, such as aerospace, medicine, food, and construction. It is particularly useful for low production volumes, low material waste, and frequent design changes. Furthermore, it provides the possibility of producing complex components by overcoming the design constraints associated with traditional manufacturing methods. The AM process also provides greater control over the production process parameters which in turn enables direct control of the material properties.

A growing number of AM processes with

different capabilities are already being developed [1]. There are various process parameters related to scanning speed, energy input, hatch distance, layer thickness and so on which dictate the capability of the process, as well as the final properties of the product. The additive nature of these fabrication processes has caused many concerns about the possible formation of defects and porosities resulting from deboning and mismatch among particles and layers. These imperfections mainly influence the mechanical properties of the AM products. A vast number of attempts have been made to tune the processing parameters and optimize feedstock material specification to improve the final mechanical properties of AMed products. There are particular aspects in AM processes, different from conventional processes, which may enable some modifications of the final microstructure. For instance, peculiar melting and solidification profiles followed by inherent AM heat treatments can be engineered during some of the AM processes, allowing researchers to produce parts with various structures and properties [2], whereas the occurrence of epitaxial growth of grains has been reported in many AM processing [3-5]. Nevertheless, the mechanical properties of AMed products can be explained by conventional microstructure characteristics, which include chemical composition, crystallographic texture, defects, and grain size distribution. Grain refining has been recognized as the only strengthening mechanism that does not deteriorate material elongation [6]. The Hall-Petch effect explains the increase in yield strength resulting from grain refinement. However, reducing grain size to the ultrafine and nanoscale may bring an extraordinary mechanical property. The latter is related to the different physical characteristics of these structures, which incorporate additional deformation mechanisms [7].

This work will discuss the potential and challenges of the well-known AM processes in manufacturing ultrafine/nano-grained (UNG) structures by dividing the processes into melting-based and deformation-based approaches. Moreover, the potentials and reported experimental results for the development of UNG material using the AM techniques will be reviewed, and related mechanical properties will be presented.

2. Melting-based methods

An additive manufacturing method in this category involves heating the raw materials to their melting point using a heat source. The part is manufactured by melting the feedstock material and depositing it layer-by-layer according to the predefined pattern. The two main methods in this category are directed energy deposition (DED) and powder bed fusion (PBF).

Defects commonly associated with melting-based methods include microporosity, residual stress, and microcracks. Typically, at high scan speeds and very low or very high beam powers, incomplete melting or vaporization of the powder can result in microporosity within the microstructure. Additionally, increasing the cooling rate to produce ultrafine/nanostructures may lead to residual stress and microcracks due to thermal stresses within the component. [8-10].

2.1. Powder bed fusion method (PBF)

During the powder bed fusion process, fine layers of powder are deposited onto a build plate. An energy source like a laser or electron beam selectively fuses the powder particles at specific locations defined by the desired geometry model. The printer used in this process has two chambers: the powder chamber and the build chamber (also known as the table or platform where the product is built). A blade spreads the powder across the platform, as illustrated in Fig. 1a. To achieve the appropriate height perpendicular to the horizontal plane, the powder and build chambers move along a linear axis parallel to the plate thickness [11].

Two of the most commonly used powder bed methods for additive manufacturing metal powders are electron beam melting (EBM) and selective laser melting (SLM). Fig. 1b illustrates how high-power energy sources, such as lasers or electron beams, are used to selectively melt the raw material powders. This method enables the production of parts with complex geometries and allows for fast production. Additionally, it provides the flexibility to use a wide range of materials, including pure metals and various alloys. This technique can be alternatively employed to additively joint material particles via surface melting, where heat input is controlled to achieve surface fusion sintering [12]. The latter technique is known as selective laser sintering (SLS). The quality and properties of the final product in this method are influenced by several process parameters, including beam power,

hatch distance, point distance, scan speed, layer thickness, and spot diameter, as shown in Fig. 1b. Additionally, material parameters such as shape, size, thermal conductivity coefficient, and alloying elements also play a crucial role in determining the final outcome.

2.1.1. Potentials for processing of UNG materials
2.1.1.1. Powder specifications

The characteristics of the powder, including particle size, shape, material type, and alloying elements, strongly affect the microstructure and properties of the fabricated parts. Smaller particles possess a larger surface area-to-volume ratio, which allows them to absorb more energy from lasers or electron beams, resulting in easy melting and fusion. Additionally, the surface energy in finer particles limits the grain size of solidified material [13]. In most research on producing ultrafine/ nanostructures through additive manufacturing, the powder particle size typically averages between 40 and 45 μm [14, 15]. Powders within this size range tend to have better flowability and higher density, which result in more uniform melting and solidification, leading to finer microstructures.

The reported results indicate that adding alloying elements can help convert columnar grains to equiaxed grains, create fine-grained microstructures (typically less than 20 μm), and improve mechanical properties. [16] Additionally, reinforcing particles (typically in the range of 90 to 970 nm [17]) can

be incorporated into the experimental metal, which may be designed to function either in-situ or ex-situ [18-21]. To facilitate rapid solidification, alloy elements with high thermal conductivity can be added to the feedstock powder to increase the cooling rate and, thereby, the solidification rate of the melt pool. Alternatively, alloying elements may facilitate the formation of finer grains by providing more favorable conditions for the nucleation of heterogeneous nuclei during solidification [22].

2.1.1.2. Beam power

In PBF AM, beam power, the energy delivered by a laser or electron beam to melt powdered materials, plays a crucial role in the mean size of developing grains. This parameter is realized to influence the thermal gradient and cooling rates during the solidification of the melt pool [23-26]. By reducing the laser power, a smaller melting pool is formed, resulting in a faster layer solidification, thereby promoting the development of finer grains. Based on the investigations presented in Table 1, the optimal range of beam power for achieving ultrafine/ nano microstructures in additive manufacturing, particularly in LPBF, typically falls between 180 and 400 W [17, 27]. Nevertheless, it should be noted that very low beam power gives rise to incomplete melting and solidification defects such as holes and porosity. Vise versa, excessive beam power may cause melt overheating and material vaporizing, which again leads to a defective microstructure.
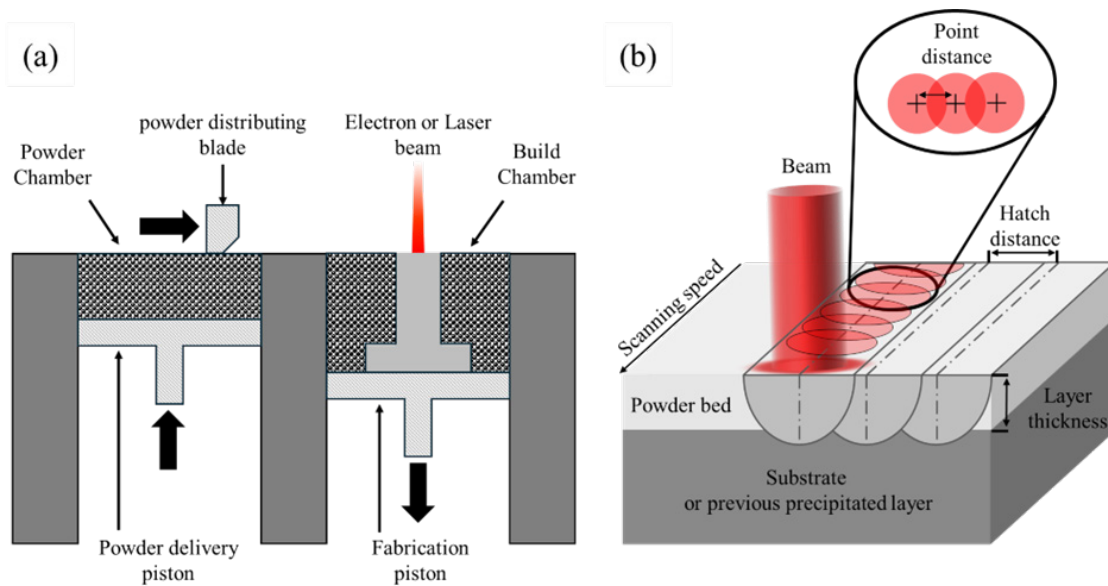

Fig. 1- Schematic of PBF methods and (b) Parameters of the PBF method..

2.1.1.3. Hatch distance and Point distance

During laser beam movement across the powder bed, hatch distance refers to the spacing between consecutive laser tracks, while point distance denotes the distance between two consecutive laser spots. In most additive manufacturing methods leading to ultrafine/nano microstructures, the hatch distance has varied from 50 to 165 μm, depending on the type of raw materials and other parameters [17, 28]. These parameters significantly impact the final piece's microstructure by dictating the thermal cycle within the molten pool and the solidification rate [29, 30]. Reducing hatch distances and point distances retains more heat in the molten pool and decreases the cooling rate, resulting in coarser and columnar grain growth. Therefore, optimizing these parameters is essential to achieve a higher solidification rate and a microstructure with fine and equiaxed grains.

2.1.1.4. Scan speed

During PBF processes (such as SLM), scanning speed refers to the speed of the laser as it moves across the powder bed to melt the powder particles. Similar to hatch distance, this parameter influences the size of the melt pool and thus alters the final grain size of the process material. As the scan speed increases, shorter interaction time between the laser and the powder bed are provided, associating with a smaller melt pool and, thereby, a higher cooling rate for the melt [14, 31, 32]. The latter provides limited time for grain growth. On the other hand, lower scan speeds provide more heat accumulation, which results in a larger molten pool and lower cooling rates. Studies have shown that the ideal scanning speed for obtaining ultrafine/nano-grained and defect-free structures falls between 500 and 1200 mm/s [14, 33].

2.1.1.5. Layer thickness

In AM methods based on PBF, "layer thickness" denotes the vertical dimension of each powder layer that is spread across the build platform and then selectively melted by lasers or electron beam. As the layer thickness has an inverse relationship with the cooling rate, a thin layer will result in faster solidification rates and, consequently, smaller grain sizes [34]. It should be noted, however, that a thinner layer thickness may result in a smoother surface but may extend the part build time. Most studies on additive manufacturing of materials with ultrafine/nano microstructures suggest that the ideal layer thickness ranges from 30 to 50 μm [28, 35].

2.1.1.6. Spot diameter

During SLM, the spot diameter indicates the diameter of the laser beam that interacts with the powder bed to melt and fuse its particles selectively. The spot diameter directly influences the heat input to the melt pool size and the dimensional accuracy of the final part [36]. Increasing the spot's diameter generates more heat, which lowers the cooling rate and allows grain growth to occur before solidification. It has been noted that a small laser diameter combined with a high scanning speed and a low laser power can produce sub-micron structures [31]. The optimal value of this parameter for achieving ultrafine/nano-grained materials in the SLM method varies between 66 to 70 μm [28, 36], However, in the SLS method, this value has been reported to be as high as 1 mm [12].

2.1.2. The obtained UNG microstructure and mechanical properties in the PBF methods

Table 1 summarizes the results of literature reports on the formation of UNG microstructures using PBF. Zafari et al. [35] demonstrated that adding Cu elements with high thermal conductivity to pure Fe creates a favorable thermal cycle during the process. This leads to liquid separation, monotectic reaction, and solid-state phase transformation, all contributing to significant grain refinement in the microstructure.

A comparison of the structure of printed pure Fe before and after the addition of Cu, shown in Fig. 2a, b, indicates that Cu increased the solidification rate and reduced the obtained grain size. A specified area in Fig. 2b (c, d) shows that the grain size near the copper fibers (d) is 250 nm, which is less than the parts far from the copper fibers (c). In a previously deposited layer, copper fibers and particles may act as nucleation sites for iron solidification, resulting in grain refinement.

Moreover, they demonstrated that the thermal cycle in SLM samples can induce rapid solidification, resulting in the dispersion of copper nanoparticles with a diameter of 5 nm within the Fe matrix at very small intervals (10 nm). As shown in Fig. 2 e, f, this process enhances strength through grain refinement and increases compressive strength from 400 MPa for SLMed Fe to 900 MPa for SLMed Fe-Cu due to the Orowan mechanism and the pining of dislocations owing to the secondary phase nanoparticles.

A study on AM of composite materials by Li et al.[37] investigated the effect of TiN nanoparticles

Table 1- Literature reports on processing of UNG microstructures using PBF

| Material	Method	Parameter	Grain size	Ref
Al-1Ti-1Sc-0.4Zr alloy	SLM	Not given	500 to 700 nm	[3]
Bulk nanostructured Al_2O_3	SLS	Laser power: 200 W Laser beam diameter: 1 mm Laser scan speed: 1500 mm/min Layer thickness: 0.5 mm	40-60 nm	[12]
Stainless steel matrix composite via vanadium carbide reinforcement	SLM	Layer thickness: 35 μm Hatch distance: 85 μm Laser power:60, 100, 140, 180, 220 W Laser scan speed: 300 and 500 mm/s	500 nm	[14]
Fe-Cu alloy	SLM	Layer thickness: 50 μm Hatch distance: 110 μm Point distance: 60 μm Laser spot size: 66 μm Laser power: 200 W	250 nm	[35]
316L/CuCrZr functionally graded materials	PBF	Layer thickness (Cu-Cr-Zn) - (316 L): 30 μm- 30 μm Hatch distance (Cu-Cr-Zn) - (316 L): 90 μm- 100 μm Point distance (Cu-Cr-Zn) - (316 L): 40 μm- 70 μm Laser power (Cu-Cr-Zn) - (316 L): 400 W-200 W	(~800 nm)	[27]
Ti-6Al-4V with additions of Fe	PBF	Layer thickness: 30 μm Hatch distance: 65 μm Point distance: 75 μm Laser power: 195 W	450 nm	[39]
Al6xxx Alloy	PBF	Not given	600 nm	[40]
Sc- and Zr-modified Al-Mg alloys	SLM	Layer thickness: 30 μm Hatch distances: 135 μm, 150 μm, 165 μm Laser spot diameter: 100 μm Laser scan speeds: 170 mm s−1 and 750 mm s−1 Laser power: 200 W	600 nm	[28]
AlSi10Mg	PBF	Layer thickness: 40 μm Hatch distance: 190 μm Laser scan speed: 900 mm/s Laser power: 370 W	0.53 to 0.93 μm	[15]
Nano-TiC reinforced Ni-based nanocomposites	SLM	Hatch distance: 50 μm Laser scan speed: 800 mm/s Laser power: 180 to 240 W Laser spot size: 70 μm	TiC size 90 to 970 nm	[17]
Al-Cu-Li-Sc-Zr alloy	PBF	Laser power: 300 W Laser scan speed: 1200 mm/s Hatch distance: 100 μm Layer thickness: 40 μm	Precipitates 75 to 125 nm	[33]
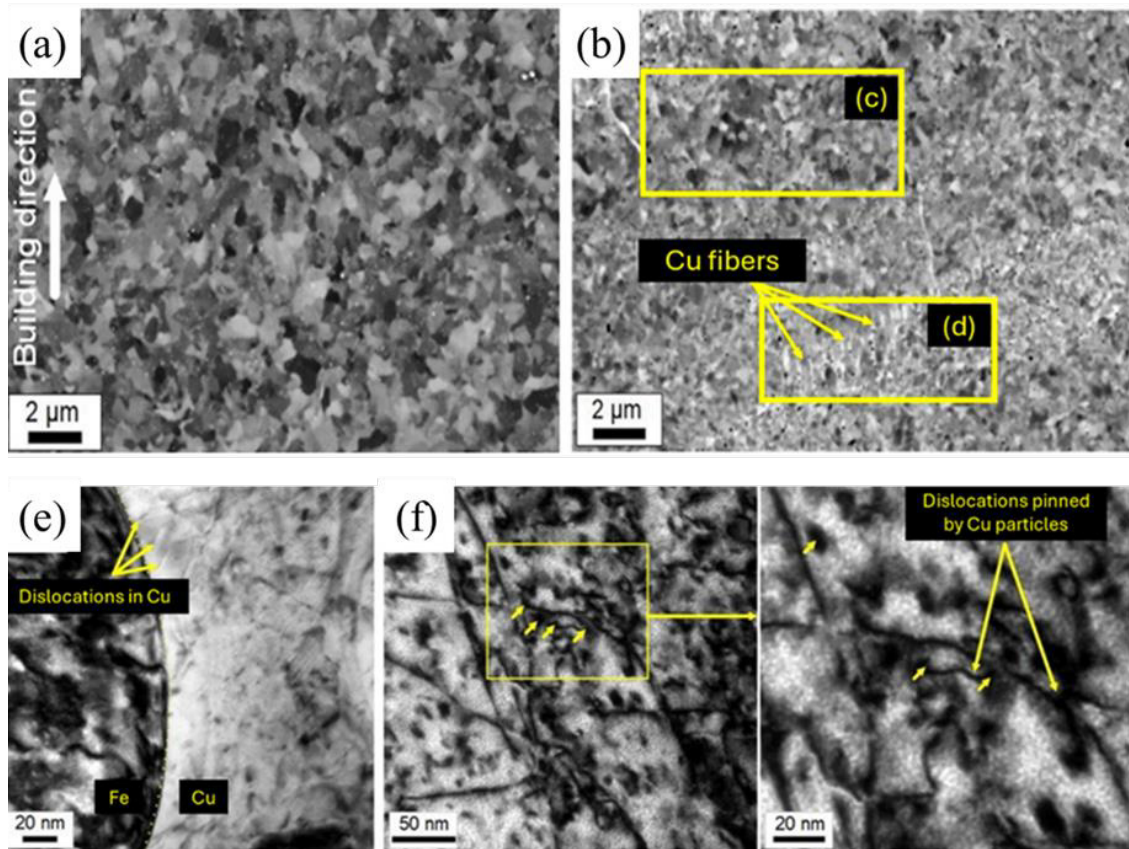
Fig. 2-(a) SEM on the as-SLM pure Fe, with grain size of ~1 μm, (b) higher resolution, showing finer Fe grains after adding Cu elements, (c) larger grains away from Cu fibers compared to (d) finer ones between them, (e) TEM of as-SLM Fe-Cu after compression showing the dislocations at the Fe/Cu-fiber interface, and (f) dislocations pinned by Cu particles [35].

(TiN_p) on the microstructure of the high entropy alloy (HEA) matrix. The TiN_p provides more heterogeneous nucleation sites, which stimulates the formation of ultra-fine and equiaxed grains (smaller than 2 μm) in the HEA matrix and the development of isotropic properties.

As shown in Fig. 3, TiN_p with their high melting points and thermal stability, are uniformly distributed throughout the microstructure, primarily at the grain boundaries of the HEA matrix. They prevent the coarsening of the grains through the Zener pinning effect and further induce grain refinement. The printed TiN_p/HEA composites exhibited enhanced strength (UTS of 1100 MPa) and improved wear resistance.

Han et al. [4] showed that a remarkable strengthening of Hastelloy X nanocomposite is obtained by grain refinement upon incorporating TiC nanoparticles during processing, which act as nucleation sites and barriers to matrix grain growth. Moreover, as shown in Fig. 4a, b, due to the difference in the coefficient of thermal expansion of TiC and the matrix, a higher dislocation density may be introduced on the particle/matrix interface in the printed samples, significantly increasing the product strength. The obtained tensile curves for the processed Hastelloy X and nanocomposite Hastelloy X are shown in Fig. 4c. Accordingly, the yield strength and ultimate strength of pure Hastelloy X were increased with the addition of TiC nanoparticles from YS:690 MPa and UTS:900 MPa to YS:810 MPa and UTS:1150 MPa respectively, though the elongation was slightly reduced from 13% to 12%.

Li. et al. [14] could control the solidification rate and matrix grain growth of 316L-based metal matrix composites (MMCs) by optimizing the SLM process parameters. In Fig. 5a, b, the microstructure of composites printed at different scan speeds were compared, revealing that higher scan speeds could yield significant grain refinement owing to a faster solidification rate and limited grain growth.
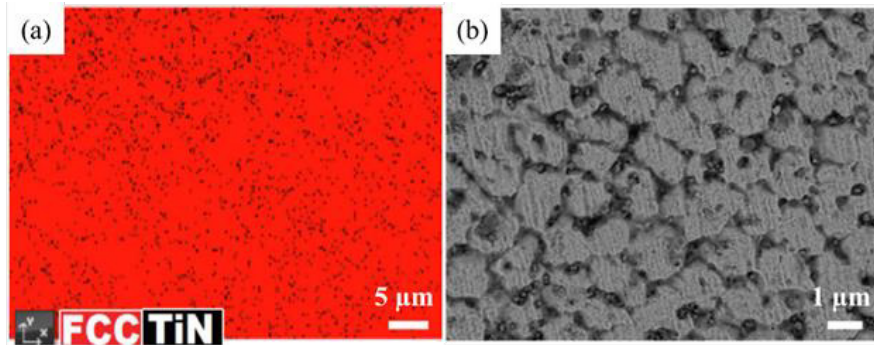
Fig. 3-(a) Phase map of printed TiNp/HEA with region colors of red (FCC phase of HEA matrix) and black (TiN phase) and (b) FE-SEM of as-printed TiNp/HEA parallel to BD [37].
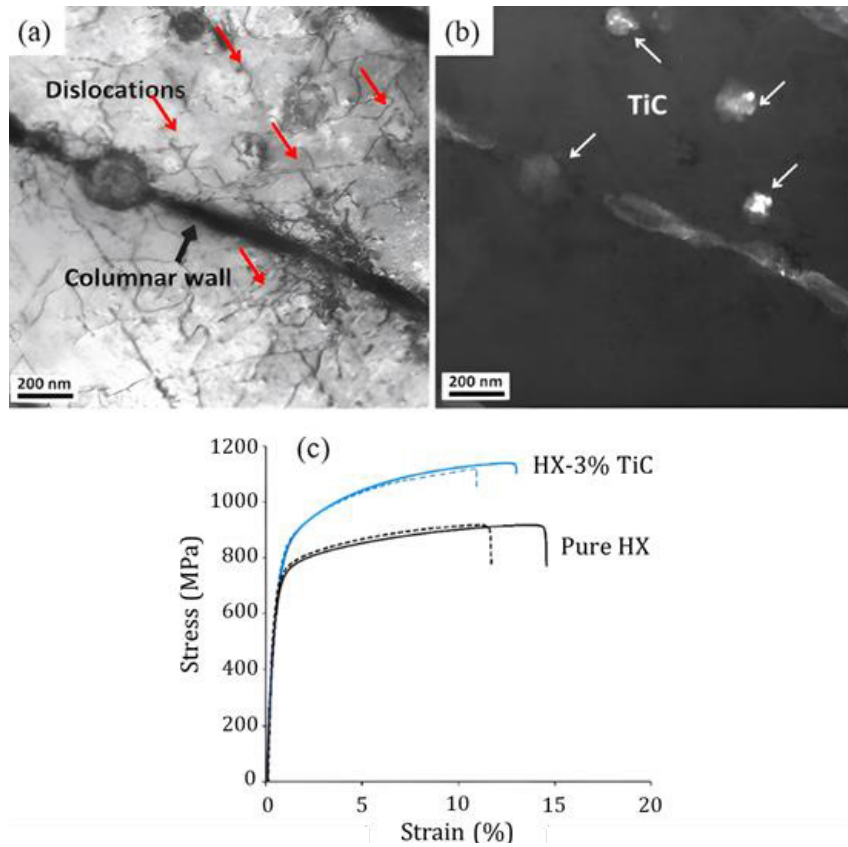

Fig. 4-(a,b) TEM images of HX-3 wt.% TiC nanoparticles, and (c) engineering stress-strain curves of the of HX-3 wt.% TiC and pure HX [4].

Furthermore, Fig. 5c, d, illustrates that adding vanadium carbide nanoparticles could promote the formation of ultra-fine structures in 316L-based MMCs by providing heterogeneous nucleation sites and barriers to further grain growth during solidification. During the SLM process, the vanadium carbide nanoparticles exert a pinning effect on the austenite grain boundaries due to the rapid solidification speed and the formation of a vanadium solid solution, resulting in a microstructure of ultra-fine and coaxial grains. A doubled tensile strength of 1400 MPa was obtained for the processed 316L/carbide composite compared to the processed 316L steel. Nevertheless, this was accompanied by a decrease in ductility from approximately 32% to 18%.
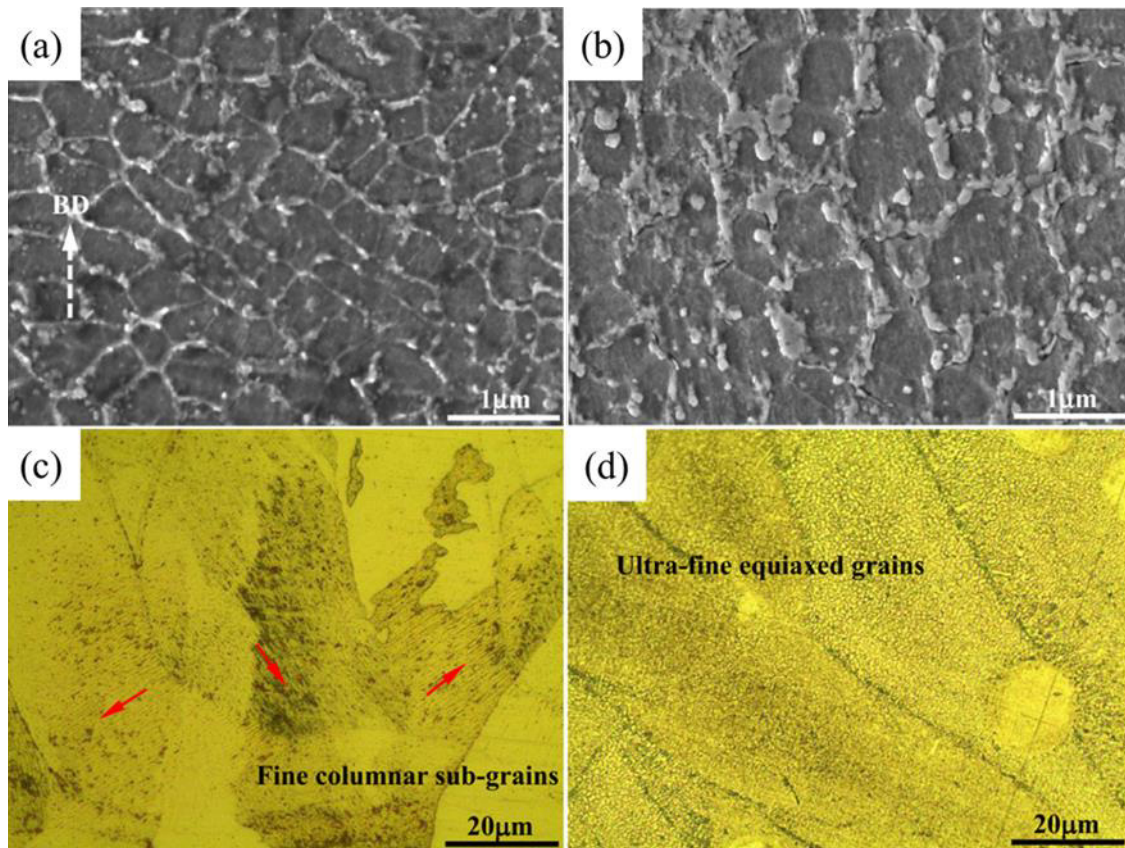
Fig. 5-FE-SEM microstructure of printed 316L-based MMCs scanned at (a) 500 mm/s, (b) 300 mm/s, and Comparison of the microstructure of (c) the as-printed 316 L sample without vanadium carbide reinforcing nanoparticles and (d) the sample containing vanadium carbide particles [14].

In the selective laser sintering (SLS) additive manufacturing method, the sintering nature of the process results in less heat input than SLM methods. This inhibits grain growth in the microstructure of the manufactured part. Furthermore, research by Shen et al.[12] indicates that using nanoscale Al_2O_3 particles (with an average size of 500 nm and primary grain size of 50 nm) in the SLS method helps to reduce further the heat input required to fabricate parts and prevents grain growth during the process and keeps the grain size below 100 nm which according to the Hall-Patch effect, will lead to better mechanical properties such as high hardness and fracture toughness.

Investigations show that fusion-based additive manufacturing methods produce parts with columnar grains and a preferred texture of <100> in the build direction, particularly in materials with a face-centered cubic (FCC) structure. As discussed in the reviewed papers, optimizing parameters can transform coarse columnar grains into fine equiaxed grains with random grain orientation. This transformation reduces the texture and anisotropy of the microstructure, often resulting in increased tensile strength and yield stress of the fabricated samples [4, 38].

2.2. Directed energy deposition (DED)

During DED, high energy density heat sources (lasers, electron beams, or plasma/electric arcs) heat the substrate and melt the feedstock material, which is delivered into the melt pool as powder or wire. The details of the processes are schematically presented in Fig. 6. A metal track is formed as the deposited metal solidifies on the substrate as the heating source moves forward. Following the predefined hatch spacing, the metal tracks overlap each other. Although the dimensional accuracy of the products made by DED is inferior to those of PBF, it presents a remarkably higher deposition rate. In this category, different techniques have been introduced based on the types of feeding material,
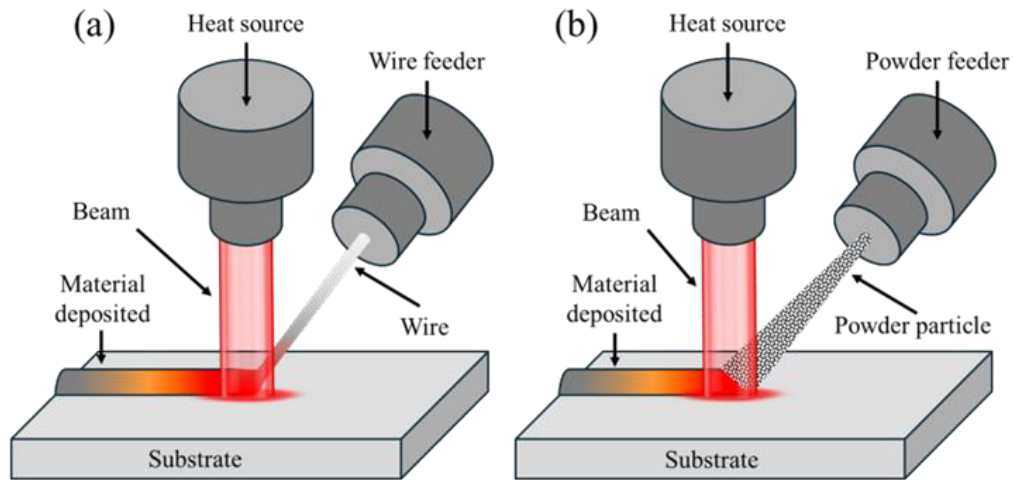
Fig. 6- Schematic of DED methods. (a) powder feed material, and (b) wire filament feed material.

wire or powder, and heating sources, including wire arc additive manufacturing (WAAM), laser wire deposition (LWD), laser metal deposition (LMD), and laser additive manufacturing (LAM). The features of the final microstructure in this method are mainly affected by the process parameters, including beam power, scan speed, spot diameter, feed rate, and feedstock material properties.

2.2.1. Potentials for processing of UNG material
2.2.1.1. Type of materials

In DED methods, in contrast to PBF methods, raw material specifications like alloy type, wire diameter, alloying elements, and reinforcement particles have a great impact on the characteristics of the developed microstructure. Alloying elements in DED can promote heterogeneous nucleation and constitutional supercooling during solidification due to the partitioning of the alloying elements. This can stimulate the development of fine equiaxed grains and counteract the tendency of grain epitaxial growth, which is intrinsic in DED methods owing to the high cooling rate and the associated sharp thermal gradient [22, 41-43]. This can be considered one of the key advantages of DED processes, which can partly control the final microstructure by tuning the initial material. Furthermore, DED offers the possibility of adding reinforcing nanoparticles (1 to 100 nm) to the deposited material, which can play two important roles during microstructure development: nucleation sites during the solidification of the melt and impeding the grain boundary migration and grain growth [44-46].

2.2.1.2. Beam power

The term "beam power" denotes the amount of energy emitted from a concentrated energy source, such as a laser or electron beam, which is employed to melt the material during deposition. Beam power plays a crucial role in the grain refinement of the fabricated part by influencing the thermal gradient and cooling rates during solidification [47-50]. Insufficient laser power can result in incomplete melting of the deposited material, leading to the presence of cavities and porosity in the final piece. Conversely, excessive laser power may cause columnar grain growth in the final microstructure due to excessive input heat, evaporation, and spraying of raw materials during the process. Therefore, increasing the laser power to an optimal level can result in an ideal melting and solidification rate, producing microstructures with denser and more equiaxed fine grains. Depending on the type of raw materials (powder or wire), the optimal laser power is usually considered from 200 to 1600 W [51, 52].

2.2.1.3. Scan speed

In additive DED manufacturing, the scan speed denotes the rate at which the laser or electron beam travels along the fabrication path. This crucial factor impacts the dimensions of the molten pool and the cooling rate through the establishment of a thermal profile for the solidification of the melted material. The optimal value that is usually considered for this parameter ranges from 300 mm/s and 800 mm/min [52, 53]. Increasing scan speed at a given condition may decrease the heat input and make the melting

pool smaller [49, 50, 54, 55]. In addition, a rapid scan brings about a high thermal gradient, which may promote the formation of fine structures and mitigate the formation of undesirable columnar grains along the manufacturing direction.

2.2.1.4. Spot Diameter

The spot diameter refers to the size of the focal point where the beam interacts with raw materials. This parameter size controls the heat input for melting the material. A larger spot diameter results in higher input heat, leading to the coarsening of microstructure grains. Conversely, a smaller spot diameter reduces the heat input to the molten pool, causing the previously deposited layers to solidify faster, which promotes grain refinement in the microstructures during the process. In the DED method, the optimal value of this parameter has a broader range compared to SLM, typically ranging from 50 μm to 1.5 mm according to various studies [41, 51].

2.2.1.5. Deposition Rate

The deposition rate, largely dependent on the feed rate, refers to the amount of material deposited onto a substrate or previously deposited layer over a given time. The material deposition rate can impact the thermal gradient and cooling rate, thus influencing the grain refinement of the deposited layers. A higher deposition rate typically results in forming a larger melt pool due to the larger deposition volume of feed materials per unit of time. As a result, the deposition temperature increases and the cooling rate decreases. Conversely, reducing the deposition rate leads to a higher cooling rate, which facilitates the achievement of finer-grained structures [56, 57]. This parameter in melting and deformation-based methods typically varies from 0.1 to 10 kg/h, depending on factors such as beam power, scan speed, feed rate, and the type of raw material. Generally, deformation methods exhibit higher deposition rates than melting methods. This is because melting methods produce parts with greater precision and more complex geometric dimensions, which results in lower deposition rates in these processes [58-60].

2.2.2. The obtained UNG microstructures through DED process

Results reported in the literature on the formation of UNG microstructures using the DED process are summarized in Table 2, which are

mainly limited to Inconel, Ti, Al alloys, and W-Fe composites. Wang et al. [19] demonstrated that adding Fe elements to a Ti-6Al-4V alloy results in the formation of semi-coherent TiFe phases (500 nm), which serve as suitable nucleation sites for crystallizing fine grains. Furthermore, adding Fe can increase the constitutional supercooling ahead of the solid-liquid interface. This promotes heterogeneous nucleation in this region, which stimulates the formation of nanograins of alpha phase rather than columnar grain growth. Fig. 7 a, shows the microstructure of Ti-6Al-4V-3.3Fe deposited through the DED process, containing nano TiFe phase particles. Also, they demonstrated that incorporating an optimal amount of iron elements (3.3 wt.%) can optimize the mechanical properties of the processed material such as hardness, yield strength, and ductility. The related mechanical behaviors under compressive loading were illustrated in Fig. 7 b.

This was discussed relying on the Orowan strengthening effect of TiFe particles within the fine-grained matrix and the solid solution strengthening of iron in titanium structure. It was highlighted that increasing the amount of Fe elements up to 3.3 wt.% leads to substituting columnar grains with equiaxed ones, which causes the plastic strain to increase from 24% for Ti-6Al-4V to 43% for Ti-6Al-4V-3.3Fe. Nevertheless, higher Fe element content (4.7 wt.%) may deteriorate the ductility due to an increased fraction of second-phase particles.

Zhang et al. [41] added copper to titanium to create a columnar-to-equiaxed transition in the microstructure of the Ti-Cu alloy system. The addition of Cu element can vanish the negative effect of the high thermal gradient in the molten pool on promoting epitaxial growth. This encourages the formation of equiaxed grains rather than columnar grains. accordingly, due to the decrease in the diffusion rate of atoms during rapid solidification, ultra-fine eutectic with a size less than 500 nm was formed.

Previous results demonstrated that adding fine particles to the melting pool during DED can be considered to fabricate AMed nanocomposites. Incorporating TiC particles into the DED processed materials was conducted to manufacture Al-based [51] and Inconel-based [53] alloys. Hong et al. [53] demonstrated that increasing the laser power for manufacturing Inconel matrix composites reinforced with ultrafine TiC particles (~200 nm in size) may result in surface melting and, thereby,

Table 2- Literature reports on processing of UNG microstructures using DED

Material	Method	Parameter	Grain size	Ref
Ti-6Al-4V alloy	LWD	Laser power: 3300 KW Wire feed: 0.064 m/s Deposition speed: 0.026 m/s Focal offset distance: 20 mm Thickness of deposition layer: 900 μm	500 nm	[19]
Ti-Cu alloy	LMD	Laser power: 800 W Scan speed: 800 mm/min Laser spot size: 1.5 mm Powder flow rate: 2.0 RPM Hatch distance: 1.05 mm	Eutectoid < 500 nm	[41]
Aluminum matrix nanocomposites reinforced with (TiC)	LAM	Power: 200 W Scan speed: 0.2 m/s Spot size: 50 μm Hatch distance: 30 μm	331 nm	[51]
Ultrafine TiC particle-reinforced Inconel 625	LMD	Powder feeding rate: 2.4 g/min Laser spot diameter: 1 mm Laser scan speed: 800 mm/min Laser power: 500 and 800 W	TiC 200 nm	[53]
W–Fe composites	LMD	Laser spot diameter: 3.5 mm Laser power: 1000–1600 W Scan speed: 300–600 mm/s Scan hatch spacing: 0.8–1.3 mm Layer thickness: 0.4–0.7 mm.	Fe_2W 200-600 nm	[52]
Al-5.0 Mg alloy	WAAM	Wire feed speed: 7.5 m/min Travel speed: 0.6 m/min Heat input: 237.13 J/m Current: 168 A Voltage: 16.9 V	100–200 nm	[63]

a reduction in the size of the TiC particles. This led to a better dispersion of these particles in the molten pool, thereby raising the nucleation rate for solidification and refining the matrix grain structure.

One key effect during DED is the potential for microstructural modification that may result from heat exposure of the deposited material due to the layer-by-layer fashion of melt-induced printing. The possible grain growth complicates the achievement of UNG microstructure. However, in age hardenable alloys, the heat treatment may stimulate the formation of ultrafine/nanoparticles. Chen et al. [52] demonstrated that the multiple thermal cycles during the course of the process

led to a solid-state phase transformation in a previously deposited layer during the production of W-Fe composites. This process forms Fe_2W precipitate with a size ranging from 200-600 nm. It was demonstrated that the latter precipitates and increases the compressive yield strength up to 1700 MPa in the printed W-Fe composite.

Research indicates that in order to achieve finer microstructures with improved mechanical properties, external factors such as ultrasonic waves and magnetic fields can be used in addition to specific parameters of each method in melting processes. Applying a magnetic field to the molten pool can help break down the dendrites formed during solidification, providing more
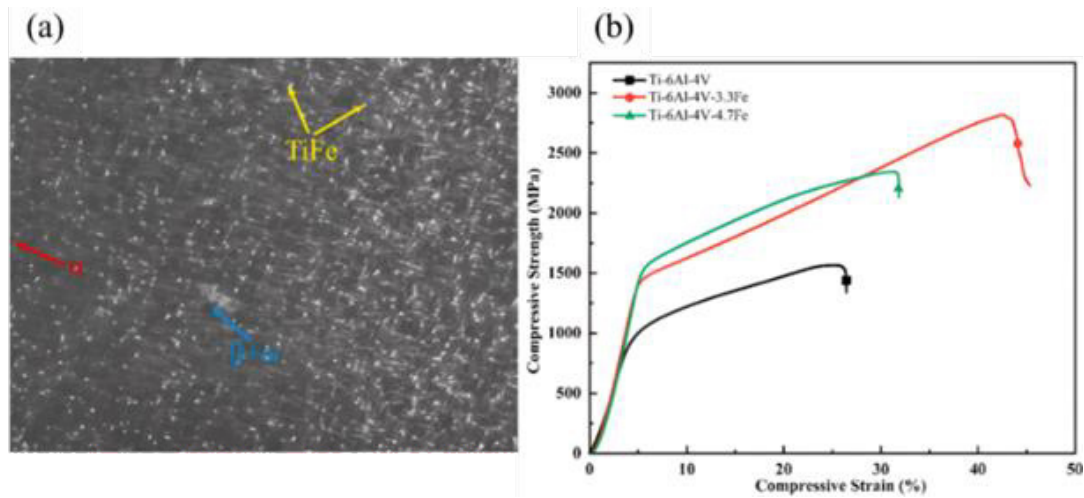
Fig. 7-(a) SEM image of the DED processed Ti-6Al-4V-3.3Fe, and (b) Compressive engineering stress-strain plots of the DED processed Ti-6Al-4V, Ti-6Al-4V- 3.3Fe, and Ti-6Al-4V-4.7Fe [19].

heterogeneous nucleation sites to achieve finer-grained structures. High-intensity ultrasonic waves (around 20 kHz) applied to the molten pool can release more gas bubbles trapped in the melt, leading to reduced porosity in the processed part and improved mechanical properties [61].

Todaro et al. demonstrated that the application of ultrasound waves during the fabrication of 316L stainless steel led to more heterogeneous nucleation and reduced grain size from 52 to 16 μm by increasing constitutional supercooling during solidification [62].

3. Deformation based methods

Additive manufacturing techniques that utilize deformation are based on the principle of plastic deformation, which involves altering the shape of a material without melting. In contrast to fusion-based methods where materials are liquefied and then solidified to form joints, deformation methods maintain the solid-state nature of the material throughout manufacturing. We will discuss two of these methods, Friction stir additive manufacturing (FSAM) and Cold spray additive manufacturing (CSAM) along with their potential to achieve UNG microstructures in the following sections.

In deformation methods, similar to melting techniques, metallurgical defects such as micropores and cracks may occur, but the causes of these defects differ. Both methods are susceptible to porosity in their structures. In melting methods, gas porosity often forms during solidification of the melt, while in deformation methods, cavities arise

from insufficient plastic deformation of the raw materials. Since these processes occur in a solid state, this type of defect is more prevalent in them. Additionally, deformation methods generally involve less heat input compared to melting methods, which reduces the occurrence of defects caused by solidification and thermal stresses [59, 64].

3.1. Friction stir additive manufacturing (FSAM)

FSAM is a process that combines friction stir welding (FSW) with additive manufacturing (AM). To join and build up material layers in FSAM, a rotating tool with a pin and shoulder is used, instead of melting and solidifying them. As shown in Fig. 8 multiple sheets are placed on top of each other and welded using the friction stir method, which creates uniform microstructures with enhanced mechanical properties along the connection. Another common additive manufacturing method based on FSW that produces ultra-fine nano microstructures (average grain size ~810 nm for nanodiamond reinforced AA6061 matrix composite coatings [65]) is additive friction stir deposition (ASFD). This method uses feedstock materials in the form of rods or wires, fed through a rotating tool, undergoing plastic deformation due to frictional heating, and deposited layer by layer in a solid-state process [66]. In FSAM, several parameters can influence the final grain structure. These parameters include tool geometry, tool rotation speed, traverse speed, process temperature, layer thickness, and material properties.
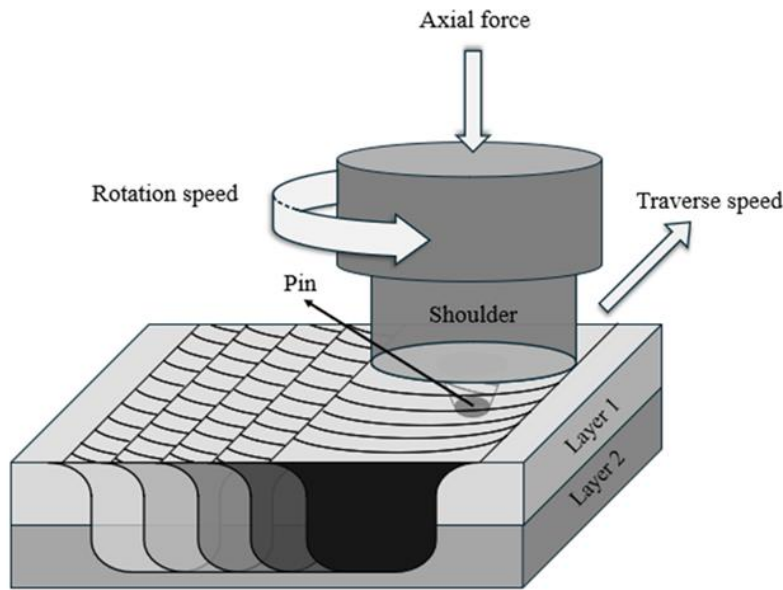
Fig. 8- Schematic representation of FSAM method.

3.1.1. Potentials for processing of UNG material
3.1.1.1. Tool Geometry

FSAM tool geometry directly impacts material flow, deformation, and heat generation during processing, which in turn affects the size of grains developed in the microstructure. The optimization of tool geometry parameters is essential for achieving desired grain sizes and mechanical properties in FSAM-processed parts.

During FSAM, material flow is greatly influenced by the shape and size of the pin at the end of the rotating tool. If the pin diameter is greater, more plastic deformation and mixing will occur, resulting in a finer grain size. Furthermore, a larger shoulder diameter can provide greater support and pressure to the material, which can facilitate plastic deformation and grain refinement. Additionally, the tilt angle of the tool relative to the material surface alters the flow pattern and shear strain imposed during the process.

3.1.1.2. Traverse Speed

The traverse speed in FSAM refers to the rate at which the rotating tool moves across the material surface during deformation, which directly dictates the material strain rate and typically range from 50 mm/min to 5 mm/s [67, 68]. The transverse speed influence indirectly influences the adiabatic heat generation and, thereby, the temperature met during the process. It is well known that increasing the strain rate and decreasing the temperature may lead to the development of finer grain sizes during deformation [69, 70]. Moreover, lower traverse speeds allow the material to flow around the rotated tool for a longer period of time, leading to improved grain refinement and uniform grain distribution throughout the fabricated part.

3.1.1.3. Layer Thickness

In the FSAM process, a thick layer retains more heat due to its higher thermal mass. Thus, heat dissipation from thicker layers may be slower than from a thinner one, resulting in higher material interface temperatures. Higher processing temperatures can be associated with larger grain sizes. In studies that successfully achieved ultrafine nanostructures using the FSAM method, this parameter ranges from 0.5 to 2 mm [67, 71].

3.2. Cold spray additive manufacturing (CSAM)

As schematically illustrated in Fig. 9, during CSAM particles are accelerated with compressed gas as a propellant through converging and diverging nozzles and reach ultrasonic speeds (usually 300 to 1200 meters per second). Two types of precipitation occur during CSAM: the formation of the initial layer precipitate, which includes the bond between the particles and the substrate, and the deposition of higher layers, which includes the bond between the particles themselves. The initial
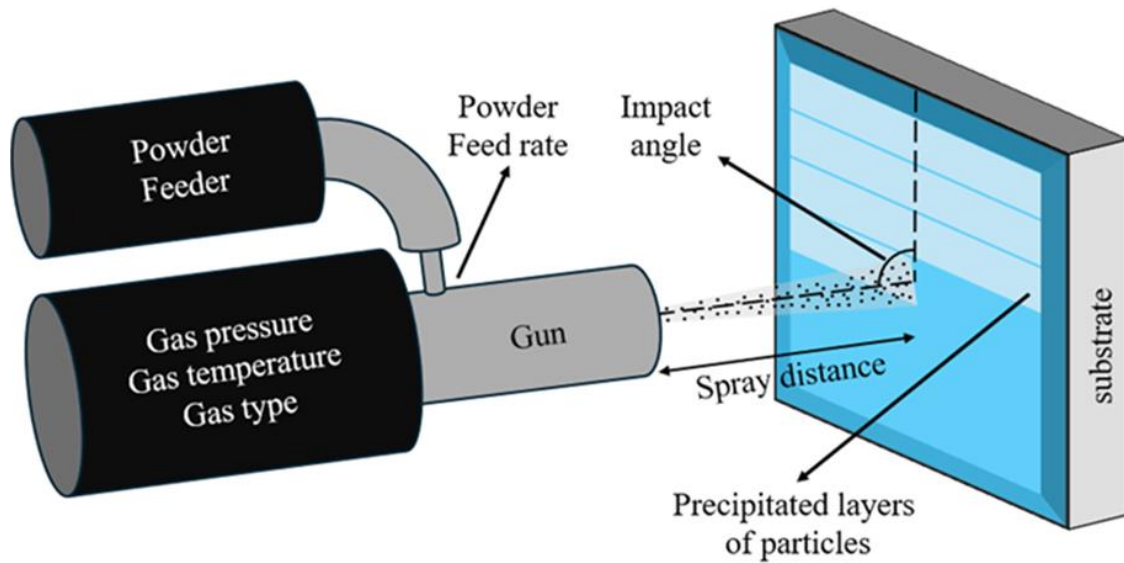
Fig. 9- Schematic of CSAM method.

speed of the particles must be greater than the critical speed specified for the particles to produce local metallurgical bonding and acceptable mechanical interlocking between the precipitate particles. Indeed, the kinetic energy of the particles is converted into plastic deformation when they strike each other or the substrate, resulting in severe plastic deformation with strain rates as high as 10^6 to 10^9 s^{-1} [72]. Low working temperatures in this method are expected to reduce or eliminate undesirable features such as oxidation, phase transformations, and grain growth compared to melting-based additive manufacturing processes.

Several parameters can influence the grain structure produced by CSAM, including particle size and morphology, particle velocity, substrate temperature, gas temperature and pressure, and impact angle. The effects of the parameters on the production of UFGs are briefly dealt with below.

3.2.1. Potentials for processing of UNG material
3.2.1.1. Particle Size and Morphology

This parameter typically ranges from 5 to 50 μm [72] and a smaller particle size obviously may result in a finer grain size in the deposited material. This is related to a greater surface area-to-volume ratio offer by finer particles, resulting in more efficient plastic deformation and bonding during impact. The deformation dislocation generated during deformation can be restored as sub-grains, which can be evolved into new fine grain upon

further straining [64]. Particles with high aspect ratios (elongated or needle-like particles) may align preferentially during impact, affecting the direction in which the material flows and how the grain grows. Accordingly, grain sizes can vary in different directions, resulting in anisotropic grain structures. Furthermore, particle surface roughness contributes to particle adhesion and inter-particle bonding during impact. By providing more bonding sites, rough surfaces may facilitate grain refinement and enhance the mechanical properties of the deposited material.

3.2.1.2. Particle velocity

With higher particle velocities, there is an increase in kinetic energy upon impact, resulting in more significant plastic deformation of both the particles and the substrate. Therefore, increased particle velocity introduces greater deformation at high strain rates. This invokes high dislocation densities and finer grain sizes upon subsequent restorations.

3.2.1.3. Substrate temperature

Substrate temperature in CSAM refers to the temperature of the substrate material during the deposition process. The higher substrate temperature may promote the occurrence of thermally activated processes in the deformed particles, resulting in the accelerated evolution of the substructure. This can end up in the rapid

formation of new grains and provide sufficient ring force for grain growth. Accordingly, the development of the UNG structure may be favored by lower substrate temperatures.

3.2.1.4. Gas temperature and pressure

Gas temperature and pressure are critical parameters influencing the deposition process, quality, and properties of parts manufactured by CSAM and typically ranges from 25 to 800°C [68, 72]. The gas pressure is carefully controlled as it directly determines the particle impact velocity, which is crucial for achieving ultrafine grain microstructure and typically ranges from 1.8 to 5 MPa [73]. Accordingly, one may expect to achieve UNG microstructure with higher gas pressure. However, as the gas temperature increases, the strength of the particles decreases, and the particles may be deformed more easily. This can yield a drop in the dislocation density produced within particles. Then, similar to the substrate temperature, a higher temperature will increase the driving force for grain

growth. Accordingly, it can be concluded that the lower the gas temperature, the finer grain structure would be expected.

3.2.1.5. impact angle

This parameter refers to the angle at which the powder particles impact the substrate or previously deposited particles. The impact angles closer to 90 would guarantee a more homogenous microstructure with higher surface quality [74]. Such conditions also cause high-impact energy and, thereby, generation of higher dislocation density within the powder, which favors finer grain structure.

3.2.2. The UNG microstructure obtained through deformation-based method

The results of research in the literature concerning the creation of UNG microstructures utilizing FSAM and CSAM techniques are outlined in Table 3. Liu et al. [67] investigated the production of three-dimensional large-scale ultrafine-grained pure copper using a novel FSAM

Table 3- Literature reports on processing of UNG microstructures using CSAM and FSAM

Material	Method	Parameter	Grain size	Ref
Pure Cu	CSAM	Propelling gas: He Gas temperature: 800 °C Gas pressure: 2 MPa Stand-off distance: 30 mm Spray angle: 90° Nozzle traverse speed: 100 mm/s Hatch distance: 2 mm	829 nm	[72]
Pure copper	FSAM	Rotation rate: 600 RPM Travel speed: 50 mm/min Tilt angle of the tool: 3° Plunge depth: 0.2 mm Sheet thickness: 2.8 mm	PZ, TZ-Y and TZ-Z ~450 ~410 ~430 nm	[67]
Al metal matrix composite	CSAM	Air temperature: 25 °C Air Pressure: 90 psig Nozzle traverse speed: 15 or 5 mm/s Stand-off distance:10 mm Ar carrier gas pressure: 60 psig Powders fed rate: 60 flow meter reading	<50 nm	[68]
Al-Zn-Mg-Cu (7075Al) reinforced with TiB2	CSAM	Standoff distance: 30 mm Traverse speed: 100 mm/s Deposition angle: 90° Propelling gas: Air, N_2, He Carrier gas: Ar, N_2, He Gas pressure: 3, 5, 1.8 MPa Gas temperature: 550, 500, 320 °C	525-958 nm	[73]

technique. This method included fast cooling with water to prevent grain growth and achieve a nano-grain size microstructure. Fig. 10 shows the grain size distribution in the related processing zone (PZ), transverse zone-Y (TZ-Y), and transverse zone-Z (TZ-Z), with average grain sizes of 450 nm, 410 nm, and 430 nm, respectively.

The relatively smaller grain sizes in the TZs are attributed to lower temperatures at the edge and bottom of the PZ, resulting from the cooling effect of flowing water. A nearly homogeneous dynamically recrystallized (DRX) microstructure was observed in the bulk UFG pure copper, resulting in excellent mechanical properties. The initial yield strength of the base material (BM) of 271 ± 4 MPa, was enhanced to a high yield strength of approximately 449 ± 7 MPa, and 456 ± 1 MPa in the FSAM-Y and FSAM-Z directions.

Chen et al.[72] reported that a pure copper with high strength and ductility was produced using CSAM, characterizing with a mean grain size of 820 nm. The processes copper exhibited impressive mechanical properties, of an ultimate tensile strength of 271 MPa, a fracture elongation of 43.5%, and a uniform elongation of 30%. Detailed analyses of individual splats revealed a gradient nano-grained (GNG) structure developed due to high-speed impact deposition (Fig. 11). These GNG-structured splats acted as building blocks for a heterogeneous microstructure with a bimodal grain distribution during the successive CSAM deposition process. The study demonstrated that CSAM could achieve synergistic strengthening and ductilization by effectively controlling grain refinement and dislocation density.
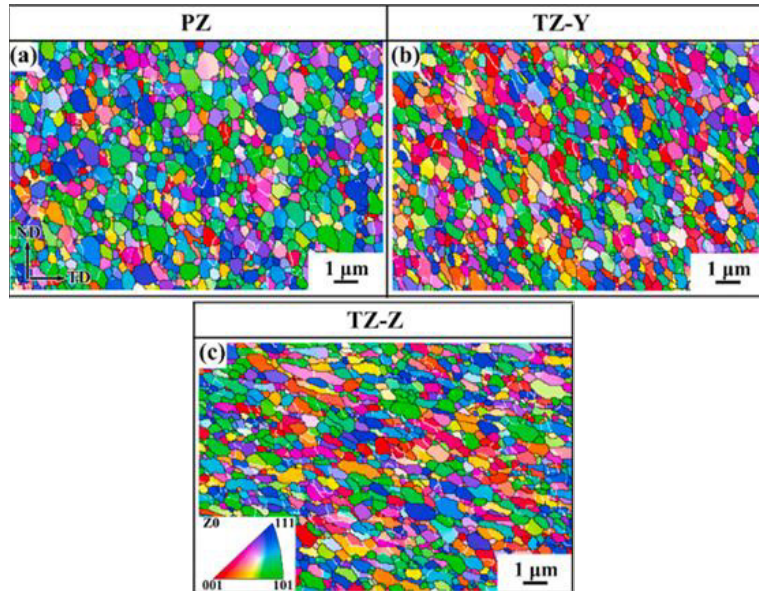

Fig. 10- EBSD microstructures of different regions in FSAM Cu sample: IPF maps of (a) PZ, (b) TZ-Y, and (c) TZ-Z regions [67].
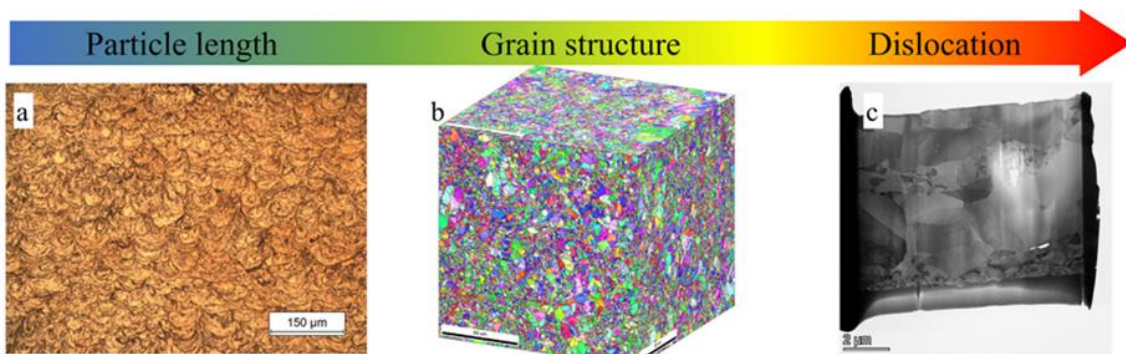

Fig. 11- Multi-scale microstructure observation of the CSAM Cu. (a) OM of the etched sample showing the severely deformed particles, (b) 3D EBSD-IPF image illustrating the heterogeneous grain structure, and (c) TEM thin-foil showing the mixture of nano and micro-scale grains [72].

4. Conclusion

The present paper aims to provide an overview of additive manufacturing methods and their potential for producing ultrafine/nano-grained materials. Accordingly, the corresponding methods are categorized into melting-based and deformation-based. It is discussed that melting-based techniques, including powder bed fusion and directed energy deposition, may be capable of producing fine-grained structures by tuning the process parameters such as beam power, point distance, scan speed, and spot diameter. Lower power and higher scan speed are associated with reduced heat input, resulting in smaller melt pools and, thereby, faster solidification rate and finer grains. FSAM and CSAM methods are considered deformation-based methods. In the former, lower traverse speeds and longer dwell times lead to the imposition of higher strain, which subsequently yields a microstructure with finer grains. In the latter deformation-based process, smaller particle sizes and higher particle velocities increase the kinetic impact energy of particles, which, in turn, introduces higher strain magnitude and dislocation density, eventually producing finer grains. The review concludes that compromising the processing parameters in melting- and deformation-based additive manufacturing methods offers great potential for producing ultrafine/nano-grained microstructures. The reported results in the literature on achieving such microstructure are summarized and discussed.

References

1. Bhatia A, Sehgal AK. Additive manufacturing materials, methods and applications: A review. Materials Today: Proceedings. 2023;81:1060-7.

2. Mukherjee T, Elmer J, Wei H, Lienert T, Zhang W, Kou S, et al. Control of grain structure, phases, and defects in additive manufacturing of high-performance metallic components. Progress in Materials Science. 2023:101153.

3. Schimbäck D, Mair P, Bärtl M, Palm F, Leichtfried G, Mayer S, et al. Alloy design strategy for microstructural-tailored scandium-modified aluminium alloys for additive manufacturing. Scripta Materialia. 2022;207:114277.

4. Han Q, Gu Y, Huang J, Wang L, Low KW, Feng Q, et al. Selective laser melting of Hastelloy X nanocomposite: effects of TiC reinforcement on crack elimination and strength improvement. Composites Part B: Engineering. 2020;202:108442.

5. Haghdadi N, Ledermueller C, Chen H, Chen Z, Liu Q, Li X, et al. Evolution of microstructure and mechanical properties in 2205 duplex stainless steels during additive manufacturing and heat treatment. Materials Science and Engineering: A. 2022;835:142695.

6. Carvalho AP, Figueiredo RB. An overview of the effect of grain size on mechanical properties of magnesium and its alloys.

7. Figueiredo RB, Kawasaki M, Langdon TG. The role of grain size in achieving excellent properties in structural materials. Journal of Materials Research and Technology. 2024;30:3448-62.

8. Tan JL, Tang C, Wong CH. A computational study on porosity evolution in parts produced by selective laser melting. Metallurgical and Materials Transactions A. 2018;49:3663-73.

9. Dilip J, Zhang S, Teng C, Zeng K, Robinson C, Pal D, et al. Influence of processing parameters on the evolution of melt pool, porosity, and microstructures in Ti-6Al-4V alloy parts fabricated by selective laser melting. Progress in Additive Manufacturing. 2017;2:157-67.

10. Dass A, Moridi A. State of the art in directed energy deposition: From additive manufacturing to materials design. Coatings. 2019;9(7):418.

11. Dev Singh D, Mahender T, Raji Reddy A. Powder bed fusion process: A brief review. Materials Today: Proceedings. 2021;46:350-5.

12. Shen LD, Huang Y, Tian ZJ, Hua GR. Direct fabrication of bulk nanostructured ceramic from nano-Al2O3 powders by selective laser sintering. Key Engineering Materials. 2007;329:613-8.

13. Zhao Y, Bian H, Wang H, Kenta A, Kenta Y, Chiba A. Non-equilibrium solidification behavior associated with powder characteristics during electron beam additive manufacturing. Materials & Design. 2022;221:110915.

14. Li B, Qian B, Xu Y, Liu Z, Zhang J, Xuan F. Additive manufacturing of ultrafine-grained austenitic stainless steel matrix composite via vanadium carbide reinforcement addition and selective laser melting: Formation mechanism and strengthening effect. Materials Science and Engineering: A. 2019;745:495-508.

15. Zhou Y, Ning F, Zhang P, Sharma A. Geometrical, microstructural, and mechanical properties of curved-surface AlSi10Mg parts fabricated by powder bed fusion additive manufacturing. Materials & Design. 2021;198:109360.

16. Talebi M, Razaghian A, Saboori A, Niroumand B. Effects of Cu addition and heat treatment on the microstructure and hardness of pure Ti prepared by Selective laser melting (SLM). Journal of Ultrafine Grained and Nanostructured Materials. 2023;56(2):213-23.

17. Gu D, Zhang H, Dai D, Xia M, Hong C, Poprawe R. Laser additive manufacturing of nano-TiC reinforced Ni-based nanocomposites with tailored microstructure and performance. Composites Part B: Engineering. 2019;163:585-97.

18. Mosallanejad MH, Niroumand B, Ghibaudo C, Biamino S, Salmi A, Fino P, et al. In-situ alloying of a fine grained fully equiaxed Ti-based alloy via electron beam powder bed fusion additive manufacturing process. Additive Manufacturing. 2022;56:102878.

19. Wang X, Zhang L-J, Ning J, Li S, Zhang L-L, Long J, et al. Fe element promotes the transformation from columnar to equiaxed grains and the formation of ultrafine microstructure of Ti-6Al-4V alloy by laser wire deposition. Additive Manufacturing. 2021;48:102442.

20. Yang M, Wang L, Yan W. Phase-field modeling of grain evolution in additive manufacturing with addition of reinforcing particles. Additive Manufacturing. 2021;47:102286.

21. Fereiduni E, Ghasemi A, Elbestawi M. TiB reinforced Ti-6Al-4V matrix composites with improved short-term creep performance fabricated by laser powder bed fusion. Journal of Manufacturing Processes. 2021;70:593-607.

22. Zhang D, Prasad A, Bermingham MJ, Todaro CJ, Benoit MJ, Patel MN, et al. Grain refinement of alloys in fusion-based additive manufacturing processes. Metallurgical and Materials

Transactions A. 2020;51:4341-59.

23. R. Kaschel F, Celikin M, Dowling DP. Effects of laser power on geometry, microstructure and mechanical properties of printed Ti-6Al-4V parts. Journal of Materials Processing Technology. 2020;278:116539.

24. Xiong F, Huang C, Kafka OL, Lian Y, Yan W, Chen M, et al. Grain growth prediction in selective electron beam melting of Ti-6Al-4V with a cellular automaton method. Materials & Design. 2021;199:109410.

25. Choo H, Sham K-L, Bohling J, Ngo A, Xiao X, Ren Y, et al. Effect of laser power on defect, texture, and microstructure of a laser powder bed fusion processed 316L stainless steel. Materials & Design. 2019;164:107534.

26. Agarwal N, Monu MCC, Tamil Selvam K, Obeidi MA, Brabazon D. Study of the effects of laser power and scanning speed on the microstructural morphologies and physical properties of L-PBF produced Ni52.39Ti47.61. Journal of Materials Research and Technology. 2023;27:8334-43.

27. Hu Z, Ma Z, Yu L, Liu Y. Functionally graded materials with grain-size gradients and heterogeneous microstructures achieved by additive manufacturing. Scripta Materialia. 2023;226:115197.

28. Spierings AB, Dawson K, Uggowitzer PJ, Wegener K. Influence of SLM scan-speed on microstructure, precipitation of Al3Sc particles and mechanical properties in Sc-and Zr-modified Al-Mg alloys. Materials & Design. 2018;140:134-43.

29. Zinovieva O, Romanova V, Balokhonov R, editors. Effect of hatch distance on the microstructure of additively manufactured 316 L steel. AIP Conference Proceedings; 2020: AIP Publishing.

30. Ehsan Saghaian S, Nematollahi M, Toker G, Hinojos A, Shayesteh Moghaddam N, Saedi S, et al. Effect of hatch spacing and laser power on microstructure, texture, and thermomechanical properties of laser powder bed fusion (L-PBF) additively manufactured NiTi. Optics & Laser Technology. 2022;149:107680.

31. Li Y, Song L, Xie P, Cheng M, Xiao H. Enhancing hardness and wear performance of laser additive manufactured Ti6Al4V alloy through achieving ultrafine microstructure. Materials. 2020;13(5):1210.

32. Abdelmoula M, Musinski W. Predicting and correlating melt pool characteristics with processing parameters in IN625 powder bed fusion additive manufacturing. Journal of Manufacturing Processes. 2024;121:427-45.

33. Qi Y, Zhang H, Yang X, Wang Y, Han C, Fan W, et al. Achieving superior high-temperature mechanical properties in Al-Cu-Li-Sc-Zr alloy with nano-scale microstructure via laser additive manufacturing. Materials Research Letters. 2024;12(1):17-25.

34. Hyer HC, Petrie CM. Effect of powder layer thickness on the microstructural development of additively manufactured SS316. Journal of Manufacturing Processes. 2022;76:666-74.

35. Zafari A, Xia K. Nano/ultrafine grained immiscible Fe-Cu alloy with ultrahigh strength produced by selective laser melting. Materials Research Letters. 2021;9(6):247-54.

36. Weaver JS, Heigel JC, Lane BM. Laser spot size and scaling laws for laser beam additive manufacturing. Journal of Manufacturing Processes. 2022;73:26-39.

37. Li B, Qian B, Xu Y, Liu Z, Xuan F. Fine-structured CoCrFeNiMn high-entropy alloy matrix composite with 12 wt% TiN particle reinforcements via selective laser melting assisted additive manufacturing. Materials letters. 2019;252:88-91.

38. Kok Y, Tan XP, Wang P, Nai M, Loh NH, Liu E, et al. Anisotropy and heterogeneity of microstructure and mechanical properties in metal additive manufacturing: A critical review. Materials & Design. 2018;139:565-86.

39. Simonelli M, Zou Z, Barriobero-Vila P, Tse YY. The development of ultrafine grain structure in an additively manufactured titanium alloy via high-temperature microscopy. Materialia. 2023;30:101856.

40. Hu Z, Gao S, Mikula J, Shen X, Seet HL, Quek SS, et al. Enhanced Plastic Stability: Achieving High Performance in a Al6xxx Alloy Fabricated by Additive Manufacturing. Advanced Materials. 2024:2307825.

41. Zhang D, Qiu D, Gibson MA, Zheng Y, Fraser HL, StJohn DH, et al. Additive manufacturing of ultrafine-grained high-strength titanium alloys. Nature. 2019;576(7785):91-5.

42. Zhang F, Gao P, Tan H, Li Y, Chen Y, Mei M, et al. Tailoring grain morphology in Ti-6Al-3Mo through heterogeneous nucleation in directed energy deposition. Journal of Materials Science & Technology. 2021;88:132-42.

43. Lu B, Cui X, Ma W, Dong M, Fang Y, Wen X, et al. Promoting the heterogeneous nucleation and the functional properties of directed energy deposited NiTi alloy by addition of La2O3. Additive Manufacturing. 2020;33:101150.

44. Chao Q, Mateti S, Annasamy M, Imran M, Joseph J, Cai Q, et al. Nanoparticle-mediated ultra grain refinement and reinforcement in additively manufactured titanium alloys. Additive Manufacturing. 2021;46:102173.

45. Wang X, Zhang L-J, Ning J, Li S, Zhang L-L, Long J. Hierarchical grain refinement during the laser additive manufacturing of Ti-6Al-4V alloys by the addition of micron-sized refractory particles. Additive Manufacturing. 2021;45:102045.

46. Yuan T, Ren X, Chen S, Jiang X. Grain refinement and property improvements of Al–Zn–Mg–Cu alloy by heterogeneous particle addition during wire and arc additive manufacturing. Journal of Materials Research and Technology. 2022;16:824-39.

47. Alhuzaim A, Imbrogno S, Attallah MM. Controlling microstructural and mechanical properties of direct laser deposited Inconel 718 via laser power. Journal of Alloys and Compounds. 2021;872:159588.

48. Yao XX, Ge P, Li JY, Wang YF, Li T, Liu WW, et al. Controlling the solidification process parameters of direct energy deposition additive manufacturing considering laser and powder properties. Computational Materials Science. 2020;182:109788.

49. Lee CH, Narayana P, Choi S-W, Reddy N, Kim JH, Kang N, et al. Influence of Direct Energy Deposition Parameters on Ti–6Al–4V Component's Structure-Property Homogeneity. Metals. 2021;11(6):887.

50. Narayana PL, Kim JH, Lee J, Choi S-W, Lee S, Park CH, et al. Optimization of process parameters for direct energy deposited Ti-6Al-4V alloy using neural networks. The International Journal of Advanced Manufacturing Technology. 2021;114(11):3269-83.

51. Lin T-C, Cao C, Sokoluk M, Jiang L, Wang X, Schoenung JM, et al. Aluminum with dispersed nanoparticles by laser additive manufacturing. Nature communications. 2019;10(1):4124.

52. Chen H, Ye L, Han Y, Chen C, Fan J. Additive manufacturing of W–Fe composites using laser metal deposition: Microstructure, phase transformation, and mechanical properties. Materials Science and Engineering: A. 2021;811:141036.

53. Hong C, Gu D, Dai D, Alkhayat M, Urban W, Yuan P, et al. Laser additive manufacturing of ultrafine TiC particle reinforced Inconel 625 based composite parts: Tailored microstructures and enhanced performance. Materials Science and Engineering: A. 2015;635:118-28.

54. Henriques ABB, de Aguiar PL, dos Santos RG, Miagava J, editors. Evaluation of Process Parameters Modifications on Directed Energy Deposition Manufactured Parts Obtained in a Hybrid Additive Manufacturing Machine. International

Manufacturing Science and Engineering Conference; 2022: American Society of Mechanical Engineers.

55. Chai R, Zhang Y, Zhong B, Zhang C. Effect of scan speed on grain and microstructural morphology for laser additive manufacturing of 304 stainless steel. Reviews on Advanced Materials Science. 2021;60(1):744-60.

56. Zhang P-l, Jia Z-y, Yan H, Yu Z-s, Wu D, Shi H-c, et al. Effect of deposition rate on microstructure and mechanical properties of wire arc additive manufacturing of Ti-6Al-4V components. Journal of Central South University. 2021;28(4):1100-10.

57. Valarezo A, Shinoda K, Sampath S. Effect of deposition rate and deposition temperature on residual stress of HVOF-sprayed coatings. Journal of Thermal Spray Technology. 2020;29:1322-38.

58. Soylemez E. High deposition rate approach of selective laser melting through defocused single bead experiments and thermal finite element analysis for Ti-6Al-4V. Additive Manufacturing. 2020;31:100984.

59. Hassan A, Pedapati SR, Awang M, Soomro IA. A comprehensive review of friction stir additive manufacturing (FSAM) of non-ferrous alloys. Materials. 2023;16(7):2723.

60. Zhong C, Biermann T, Gasser A, Poprawe R. Experimental study of effects of main process parameters on porosity, track geometry, deposition rate, and powder efficiency for high deposition rate laser metal deposition. Journal of Laser Applications. 2015;27(4).

61. Qi X, Liang X, Wang J, Zhang H, Wang X, Liu Z. Microstructure tailoring in laser powder bed fusion (L-PBF): Strategies, challenges, and future outlooks. Journal of Alloys and Compounds. 2024;970:172564.

62. Todaro C, Easton M, Qiu D, Brandt M, StJohn D, Qian M. Grain refinement of stainless steel in ultrasound-assisted additive manufacturing. Additive Manufacturing. 2021;37:101632.

63. Geng Y, Panchenko I, Chen X, Ivanov Y, Konovalov S. Wire arc additive manufacturing Al-5.0 Mg alloy: Microstructures and phase composition. Materials Characterization. 2022;187:111875.

64. Zou Y. Cold spray additive manufacturing: microstructure evolution and bonding features. Accounts of Materials Research. 2021;2(11):1071-81.

65. Wu B-l, Peng Y-c, Tang H-q, Meng C-c, Zhong Y-f, Zhang F-l, et al. Improving grain structure and dispersoid distribution of nanodiamond reinforced AA6061 matrix composite coatings via high-speed additive friction stir deposition. Journal of Materials Processing Technology. 2023;317:117983.

66. Yu HZ, Mishra RS. Additive friction stir deposition: a deformation processing route to metal additive manufacturing. Materials Research Letters. 2021;9(2):71-83.

67. Liu M, Wang B, An X, Xue P, Liu F, Wu L, et al. Friction stir additive manufacturing enabling scale-up of ultrafine-grained pure copper with superior mechanical properties. Materials Science and Engineering: A. 2022;857:144088.

68. Shao C, Li H, Zhu Y, Li P, Yu H, Zhang Z, et al. Nano-additive manufacturing of multilevel strengthened aluminum matrix composites. International Journal of Extreme Manufacturing. 2022;5(1):015102.

69. Huang F, Tao N. Effects of strain rate and deformation temperature on microstructures and hardness in plastically deformed pure aluminum. Journal of Materials Science & Technology. 2011;27(1):1-7.

70. Guo-Zheng Q, Yang W, Ying-Ying L, Jie Z. Effect of temperatures and strain rates on the average size of grains refined by dynamic recrystallization for as-extruded 42CrMo steel. Materials Research. 2013;16:1092-105.

71. Elyasi M, Khoram D, Aghajani Derazkola H, Mirnia MJ. Effects of process parameters on properties of friction stir additive manufactured copper. The International Journal of Advanced Manufacturing Technology. 2023;127(11-12):5651-64.

72. Chen C, Xie Y, Yin S, Li W, Luo X, Xie X, et al. Ductile and high strength Cu fabricated by solid-state cold spray additive manufacturing. Journal of Materials Science & Technology. 2023;134:234-43.

73. Xie X, Ma Y, Chen C, Ji G, Verdy C, Wu H, et al. Cold spray additive manufacturing of metal matrix composites (MMCs) using a novel nano-TiB2-reinforced 7075Al powder. Journal of alloys and compounds. 2020;819:152962.

74. Prashar G, Vasudev H. A comprehensive review on sustainable cold spray additive manufacturing: State of the art, challenges and future challenges. Journal of Cleaner Production. 2021;310:127606.